Surface Layers of Zr-18%Nb Alloy Modified by Ultrasonic Impact Treatment: Microstructure, Hardness and Corrosion

N.I. Khripta, O.P. Karasevska, and B.N. Mordyuk

Near-surface layers in Zr-18%Nb alloy were modified using ultrasonic impact treatment (UIT). The effects of the UIT processing time on a microstructural formation, omega/alpha precipitations, microhardness and corrosion are analyzed. XRD analysis, TEM and SEM observations and EDX characterization allow establishing the links between the microstructure, microhardness and corrosion behavior of the surface layers formed. At the strain extent up to $e \approx 0.3$, structural formation occurs under influence of deformation induced heating, which facilitates omega precipitation in beta phase and mechanically induced oxygen transport and oxide formation. XRD analysis reveals moderate compressive residual stresses ($- 160$ MPa) and pronounced {110} texture after the UIT process. Generation of dislocations and hindering of their movement by nanoscale omega precipitates manifest themselves as the broadening of diffraction peaks occurred mainly owing to the lattice microstrains, and they provide marked strain hardening. The enhanced anticorrosion properties of Zr-18%Nb alloy in saline solution were concluded to be a result of the formation of a protective oxide film, {110} texture and compressive stresses.

1. Introduction

In most cases, the surface roughness, microstructure, phase composition and stress state of the surface layers of metallic materials dictate their operation performance, particularly wear and corrosion resistance, and thus affect the overall operation life of metallic constructions. Therefore, an improvement of these properties by modification of metallic surfaces remains to be a task of high importance and topicality.

Zr-Nb alloys are important construction materials for energy production since they are widely used for the cladding of nuclear fuel or for the channel tubes in the nuclear power reactors (Ref 1-6). Besides, Zr alloys were recently analyzed with regard to their potential prospects in biomedical applications (Ref 7, 8), particularly considering the elements of the highest biocompatibility (Zr, Ti, Nb, Ta) (Ref 9, 10).

Depending on the alloy composition a wide variety of phase transformations can occur in Zr-Nb alloys (Ref 1, 3, 11-14). Zirconium-rich alloys containing up to 7% of niobium (the most technologically important of which are Zr-1%Nb, Zr-2.5%Nb) are characterized with substantial volume fractions of bcc β-phase (containing about 10-20% of Nb) in the hcp α matrix (with the maximum content of Nb $\leq 1\%$). The β to ω

transformation during quenching (athermal ω) or isothermal holding (isothermal ω precipitation) can occur in the Zr-Nb alloys containing 7-20% of Nb (Ref 1, 3, 12, 14). The formation of α phase can also be observed in the alloys containing the supersaturated beta phase including the alloys of eutectoid composition (18-20%Nb) (Ref 1, 15). Strain-induced β to ω and β to α transformations were also reported to occur in the severely plastically deformed (Ref 12, 15) or impact strained (Ref 16, 17) Zr-(18-20)%Nb alloys and more frequently in β titanium alloys (Ref 18-23).

Enhanced hardness and anticorrosion properties of zirconium alloys can be achieved by means of dynamic deformation (Ref 24) and various methods of surface severe plastic deformation (SPD), such as shot peening (Ref 25), SMAT (Ref 26) and UIT (Ref 17, 27, 28). Essential hardening of the surface layers of zirconium alloys was reported to occur owing to plastic deformation. Dislocation activity (Ref 29) and/or mechanical twinning (Ref 30) can facilitate the grain refinement (Ref 24, 26-30) and texture formation (Ref 27-29, 31). Thermally or strain-induced phase transformations can also play important roles in the hardening process. Besides, some studies report on superficial mechano-chemical reactions, such as the formation of intermetallic layers (Ref 26) or mechanically induced oxygen diffusion and oxide formation (Ref 32-35), which should also be considered as possible mechanisms for the surface hardening and enhanced anticorrosion performance of Zr alloys. Comparing to the Zr-1%Nb and Zr-2.5%Nb alloys, the Zr-18%Nb alloy having bcc lattice might possess higher hardness and better corrosion resistance after surface severe plastic deformation.

This study is aimed to analyze the surface layers of the Zr18Nb alloy modified using the UIT process and to find a correlation between the formed microstructures and the hardness and corrosion behaviors of the UIT-modified surfaces in a saline solution.
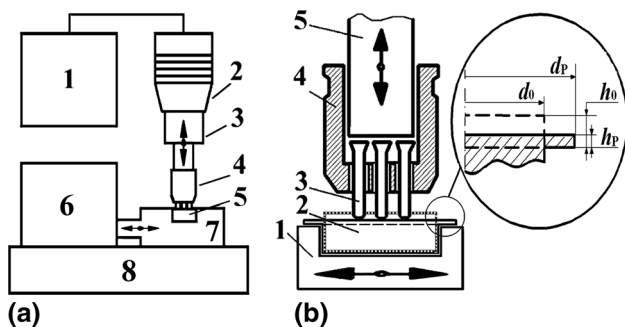
N.I. Khripta, O.P. Karasevska, and **B.N. Mordyuk,** Kurdyumov Institute for Metal Physics, NAS of Ukraine, 36 Academician Vernadsky blvd, Kiev 03142, Ukraine. Contact e-mail: mordyuk@imp.kiev.ua.

2. Experimental Details

The ingots of the eutectoid alloy Zr-18%Nb contained (in wt.%) 18.0Nb, ~ 0.15 Fe and 0.16O were hot forged and hot rolled to obtain the strips with a thickness of ~ 10 mm. Then, the oxidized surface layers were removed by mechanical polishing of both sides of the strip (to a final thickness of ~ 8 mm) and vacuum annealed (at 10^{-3} Pa at 1023 K for 2 h). The obtained strips were then cold rolled to the thickness reduction of about 75%. Further, the plain disks of 10 mm in diameter and 2 mm in thickness were cut out from the rolled strip. Finally, the specimens of Zr-18%Nb alloy were mechanically polished to a mirror finishing, heated to 1000 °C and water quenched (WQ) to fix the β-phase.

The prepared plain specimens were positioned in the socket in the reciprocating holder (Fig. 1a) and subjected to multiple impacts during the UIT process using the contact-shift loading regime (Ref 17, 27, 28). Four series of specimens (each contained three pieces) were UIT-processed for different times (0.5; 1; 2 and 4 min), and all the measured characteristics were then averaged. The relation between the normal and shear velocities of pins was sustained to be approximately constant by maintaining the appropriate frequencies and shift amplitudes of the ultrasonic horn tip (frequency f_{US} = 21.7 kHz and amplitude A_{US} = 22 μm) and the specimen holder (frequency f_{SH} = 25 Hz and amplitude A = 19 mm). In other words, the equality between the normal ($\upsilon_{\perp} = \upsilon_{us} = 2\pi f_{US}A_{US} = 2.99$ m/sec) and shear ($\upsilon_{\parallel} = \upsilon_{lfv} = 2\pi f_{SH}A = 2.98$ m/s) velocities of the pin was almost equal during each impact. Such sliding impacts (the impacts tilted at 45° to the treated surface) allow expecting substantially decreased final roughness of the processed surface.

The maximum deformation is achieved in the top surface layer. In this work, we estimate this deformation by the change of geometric dimensions of the deformed layer (Fig. 1b) (Ref 27, 28, 36):

$$\overline{e} = \frac{\sqrt{2}}{3}\left[(\varepsilon_1 - \varepsilon_2)^2 + (\varepsilon_2 - \varepsilon_3)^2 + (\varepsilon_3 - \varepsilon_1)^2\right]^{\frac{1}{2}}, \quad \text{(Eq 1)}$$

where $\varepsilon_1 = (h_0 - h_P)/h_0$ and $\varepsilon_2 = \varepsilon_3 = (d_0 - d_P)/d_0$ denote main deformations, h_0 and d_0—initial specimen dimensions, h_P and d_P—final specimen dimensions.

The temperature rise in the surface layer owing to the deformation heat ΔT was estimated as follows (Ref 24):

$$\Delta T = \frac{\eta A_D}{C_V m \rho} = \frac{\eta}{C_V m \rho} \iiint_V \sigma_T \overline{e}\, d\varepsilon, \quad \text{(Eq 2)}$$

where A_D denotes the work of deformation, HV is a microhardness (which approximately equals to the triple yield stress $HV \approx 3\sigma_T$), $\overline{e}$ stands for the deformation, C_V is the specific heat of the deformed metal, ρ stands for the specimen density, and m is a mass in the deformation zone, $\eta \approx 0.9$ denotes a conversion factor describing the part of the deformation work done converted into heat (Ref 24).

The microstructure of the surface layers of 10-20 μm thick on the UIT-processed specimens was studied using nondestructive x-ray diffraction (XRD) analysis by means of a Rigaku Ultima-IV diffractometer in Cu Kα irradiation. Assuming a biaxial stress state ($\sigma\| = \sigma_1 + \sigma_2$), analysis of residual stress was carried out using a $\sin^2\psi$-based method accounting for the elastic modulus (E = 69.62 GPa) and Poison's ratio (ν = 0.38) evaluated using the measured ultrasonic velocities. The contributions of crystallite size (D_{av}) and microstrain (η) to the broadening of diffraction profiles were estimated using a Williamson-Hall method. The microstructure in the topmost surface layer is studied by transmission electron microscopy (TEM) applying a JEOL CX-II JEM100 microscope. The plane-view TEM foils from the top subsurface layer (~ 15-20 μm) were prepared by mechanical polishing to a thickness ~ 30 μm followed by one-side electropolishing using a twin-jet technique in a solution of 400 ml CH_3OH, 240 ml $C_6H_{14}O_2$ and 40 ml $HClO_4$ at the temperature of -35 °C. Local chemical compositions of the UIT-processed surface layers were determined by the scanning electron microscopy (SEM) using JSM 6490LV microscope equipped with a nitrogen-free energy dispersion analyzer (EDA) INCA Energy 450XT. The transformation sequence in the surface layer of the UIT-processed specimen of Zr-18%Nb alloy was characterized on heating by dilatometry. The square plates (10×5 mm^2) of 200 μm thick prepared by one-side polishing were used for dilatometry. The coefficient of thermal expansion based on the dilatometry variation $\Delta l/l_0$ of the sample was obtained using homemade apparatus during continuous heating under vacuum (10^{-6}–10^{-7} mbar) with a scan rate of 5 °C min^{-1} from room temperature to 900 °C.

Microhardness HV measurements were performed using the PMT-3 microdurometer at a load of 100 g on the Vickers' indenter and at a dwell time of 10 s. The HV values averaged over ten different surface points and over three samples UIT-processed for the same time were then under consideration. To analyze the corrosion behaviors of the specimens in 3.5% NaCl water solution the potentiodynamic curves were registered using a potentiostat P5827-M connected to a three-electrode electrochemical cell with a platinum counter electrode and saturated calomel reference electrode (SCE). The following quantities were measured and estimated to characterize the corrosion behaviors of the studied specimens: the corrosion

Fig. 1 Scheme for the UIT equipment (a) consisted of ultrasonic generator (1), ultrasonic instrument (2) with ultrasonic horn (3) and the impact head (4), cylindrical specimen (5), low-frequency generator (6) with the specimen holder (7) sliding on the base plate (8) and scheme for the UIT loading cell (b): holder (1), specimen (2), pins (3), impact head (4), ultrasonic horn (5). Inset in (b) shows the dimensions of the surface layer before (d_0, h_0) and after (d_P, h_P) the UIT process

potential (E_C), corrosion current (i_C), passivation current (i_P), the breakdown potential (E_{BD}) of the oxide film and the passivity region $\Delta E_P = E_{BD} - E_C$.

3. Results and Discussion

3.1 Microstructure Observations

3.1.1 X-ray Analysis. Diffraction patterns for the specimens after water quenching and subsequent UIT process are shown in Fig. 2. Along with some broadening and shift of the main lines of β-phase, the UIT process results in the appearance of low-intensity wide reflexes in the x-ray diffraction patterns. The angle positions of some of these reflexes may correspond to the zirconium oxides or more complex ZrNb oxides. The zirconium oxide of the ZrO_2 stoichiometry has a wide variety of crystalline structures including tetragonal-ZrO_2, cubic-ZrO_2, orthorhombic-ZrO_2, hexagonal-ZrO_2 or monoclinic-ZrO_2, etc. However, the most of them can be formed at high temperature. Another recently reported possibility relates to the mechanically induced oxygen diffusion and oxide formations observed at the metallic surfaces under influence of plastic deformation or attrition (Ref 32-34). The temperature rise induced by plastic deformation owing to the transformation of the deformation work done into heat can also facilitate these processes. A thorough analysis of the registered XRD spectra and accounting for the most thermodynamically easy formed phases allow choosing three oxides, which lines matched up the experimentally registered positions of the diffraction maxima. They are denoted in Fig. 2 as (ZrNbO)O, m-ZrO_2 (monoclinic phase) and t-ZrO_2 (tetragonal phase). Additionally, some of the registered lines can be related to the ω-phase, which precipitation was described in many publications devoted to the heat treated or deformed zirconium (Ref 16, 17) and more often to the β-Ti alloys undergone severe deformation (Ref 18, 20, 21) or annealing treatment after the shock loads (Ref 19). The angle positions of the peaks seemingly related to the ω-phase are also indicated in Fig. 2. Fortunately, more reliable information regarding the ω phase formation was obtained using TEM observations and will be described in the next subsection.

Figure 3 shows the central parts of {110} pole figures for the initial and UIT-processed specimens of Zr-18%Nb alloy. In the alloys with bcc crystalline structure, the most probable rolling textures are known to have the {110} reflexes of maximum intensity (Ref 37). In this work, the initial specimen was characterized by random orientation of the grains (Fig. 3a), and the UIT process of a mild regime to the strain extent of $\bar{e} \leq 0.3$ results in significant reorientation of the grains in the surface layer (Fig. 3b). The texture of {110} type registered after UIT process is expected to be beneficial with regard to the enhanced corrosion resistance owing to the fact that the most close-packed atomic planes {110} are positioned parallel to the treated surface in this case. The most intensive (110) texture was registered in the top surface layer of the UIT-processed specimens of bcc Cr-Ni-Mo-V pressure vessel steel (Ref 38). Actually, we have the situation similar to the case of the hcp zirconium alloys severely deformed by means of compression (Ref 5, 31) or UIT process (Ref 27, 28), magnesium alloys deformed with cryogenic burnishing (Ref 39) or ECAP processed Ti alloy (Ref 40). All mentioned alloys possessed strong basal texture (0001) and were characterized by enhanced anticorrosion properties.
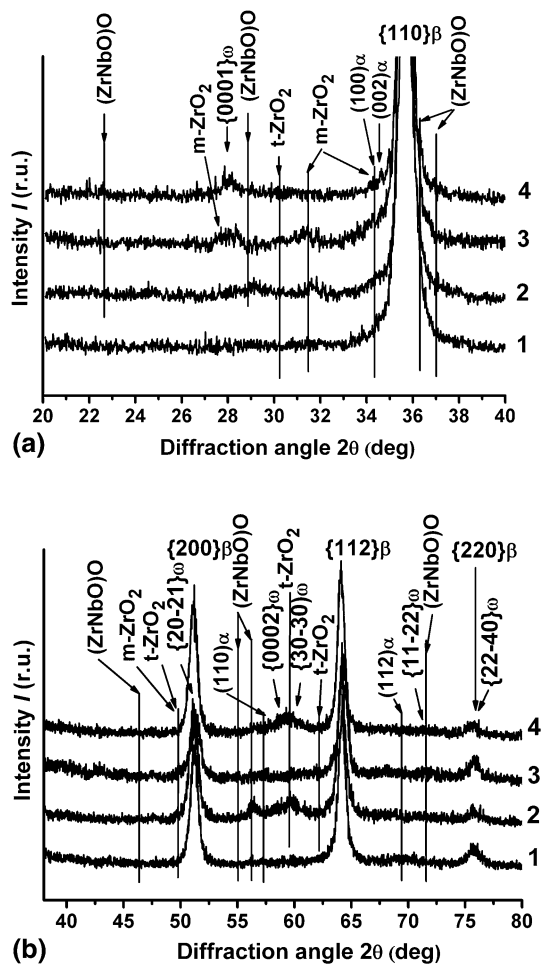

Fig. 2 Fragments of x-ray diffraction patterns registered for the initial WQ (1) and for UIT-processed specimens treated for 120 s (2), 210 s (3) and 240 s (4)

3.1.2 TEM Observations. According to the TEM analysis, the Zr-18%Nb alloy has bcc crystal structure after water quenching. The dislocation density is rather low (Fig. 4a). The SAED pattern registered with (311) β zone axis shows clear spots corresponding to the bcc lattice and some markers of the diffusive elongated spots indicating the presence of the certain areas in the β-phase lattice, which atomic configuration is inherent to the hexagonal lattice of ω-phase of athermal nature.

UIT processing for 60 s (to the effective strain of $\bar{e} \approx 0.2$) results in an essential increase in the dislocation density, and many twisted dislocations are often composed in the nets, which appear fixed with obstacles (Fig. 4b). The corresponding SAED pattern with (110) β zone axis already contains much more intensive diffusion spots in the intermediate positions between the β spots (1/3(112), 2/3(112), 1/3(114) and 2/3(114)), which are intrinsic for the ω-phase. Based on the observed SAED pattern, it can be concluded that the net of dislocations observed in the bright field images is fixed with nanoscale ω-precipitates. These nanoscale ω-precipitates cause the formation of the diffusive spots, which form an almost continuous ring in the SAED pattern.

Further increase in the UIT time to 120 s ($\bar{e} \approx 0.3$) leads to the formation of dense tangles of dislocations trapped by numerous nanoscale ω-precipitates (Fig. 4c). Appropriate SAED with (110) β zone axis contains more pronounced spots,
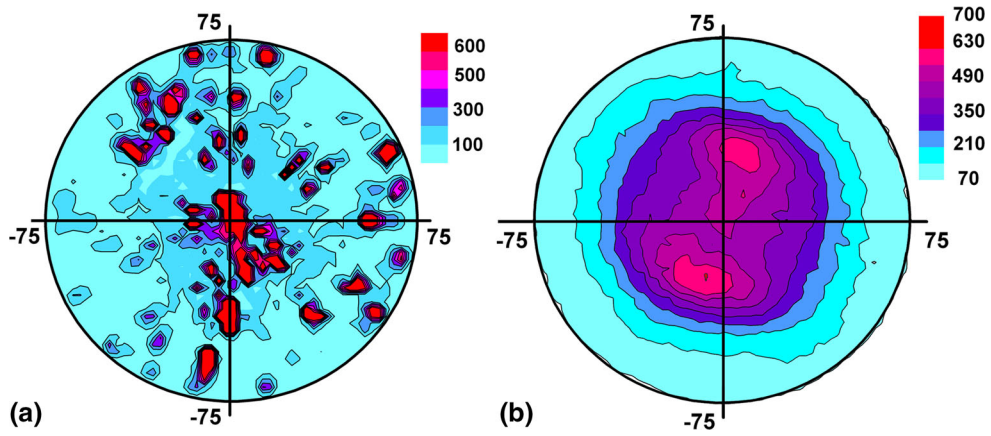
Fig. 3 {110}β pole figures for the plane specimens of Zr-18%Nb alloy in the initial (a) and UIT-processed (b) states
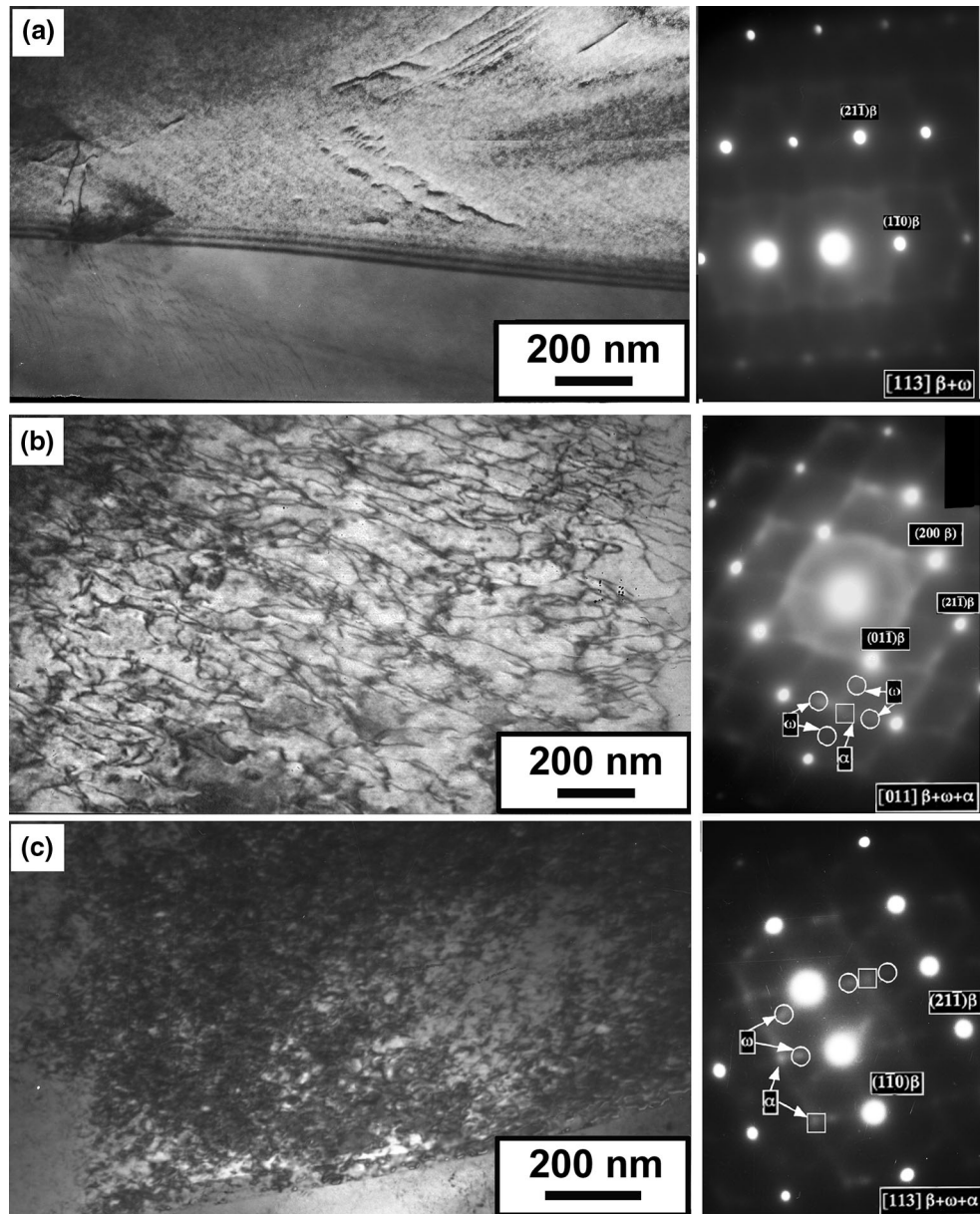
Fig. 4 TEM observations of microstructure in the surface layer of Zr-18%Nb alloy in WQ state (a) and after the UIT processes for 60 s (b) and 120 s (c)

which can be indicated as those related to both the ω- and α-phases. Typical microstructure and SAED patterns of both the UIT-2- and UIT-4-processed specimens are very similar. In this sense, these data are slightly contradictive to the results of the x-ray analysis, which have demonstrated relatively intensive diffraction maxima matching the ω-phase and only traces of the reflections from the α-phase. This fact is indicative of the insignificant volume fraction of the α-precipitates, which can be found only in local areas (seemingly in the most strained ones). The assistance of ω-precipitates in the formation of α-phase is widely discussed in the literature, particularly for the case of β-Ti alloys (Ref 18, 21, 41, 42). Thus, in our case, a lot of ω-precipitates formed during both the thermal treatment and UIT process can also assist the α-phase formation. A number of studies conclude that the α-precipitates can be nucleated either near the ω/β interface (at a certain distance from it) (Ref 21, 41) or by means of a displacive ω to α transformation within the core of the ω-precipitates (Ref 16, 18). The latter mechanism was concluded to be less probable, particularly considering many previous reports analyzed in (Ref 21, 43).

An additional factor playing pro this assistance during the UIT process is a significant increase in the concentration of vacancies by means of the movement of the screw parts of dislocations in the bcc lattice (Ref 44). The appearance of many vacancies can promote ω-precipitation because the tensile stresses formed in the bcc lattice around these vacancies or vacancy clusters can relieve the compressive stresses arisen around the ω-particle. Indeed, the unit cell volume of the hexagonal lattice (ω-phase) is lower than that of the bcc lattice (β-phase) (Ref 45). Therefore, the formed ω-inclusions induce compressive stresses in the β-matrix near the β/ω interface. These stresses may transform the coherent β/ω interface into the incoherent one, and thus lead to the stoppage/reduction of the ω-particle growth. The latter would promote nucleation of additional ω-nuclei in other sites of the bcc lattice. Therefore, numerous nanoscale ω-precipitates can be easily formed and affect the hardness of the UIT-modified Zr-18%Nb alloy. A similar mechanism was suggested previously for the formation of the ω-particles in the β-Ti alloy aged after the shock compression (Ref 19). The dynamic compression applied was also suggested to be responsible for the stimulation of high concentration of vacancies in the β-phase, which facilitated fast relaxation of the ω-phase-induced stresses.

The phase transformations occurred at the deformation process accompanied with the temperature rise can be screened out using dilatometry measurements on heating. The transformation sequence in the surface layer of the UIT-processed specimen of Zr-18%Nb alloy is shown in Fig. 5 as a variation of the thermal expansion coefficient. The metastable β phase of the Zr-18%Nb alloy dilates linearly at the initial stage due to the thermal expansion of crystal lattice by linear heating. The ω phase of athermal nature (ω_{ATH}) formed during quenching (Fig. 4a) and disappeared reversibly on heating (Ref 23) results in a slight change in the linear dependence. Then, starting from ~ 170 °C, some deviation from this linear dependence occurs because of the irreversible precipitation of the ω_{ISO} hexagonal phase, which involves diffusional phenomena. The ω precipitation process appears to be essentially accelerated at 320 °C (identified by $T\omega_{ISO}$ in Fig. 5), where a decrease is observed in the dilatometry curve. This decrease during the diffusion-controlled formation of ω_{ISO} is due to the fact that the atomic radius of Nb (1.45 Å) is smaller than the atomic radius of Zr (1.585 Å), and the rejection of the β-stabilizer alloying element

(Nb) occurs from the ω precipitates formed to the surrounding β matrix. The dilatometry curve decreases with increasing temperature reaching its minimum at ~ 400 °C.

Starting from this temperature (indicated by $T\alpha_{nano}$), the substantial increase in the dilatometry curve occurs (i.e., the sample length rapidly dilates) due to the sequential vanishing of ω_{ISO} through a ω/α phase transformation. Usually, the ω_{ISO} phase has been widely observed to act as a heterogeneous nucleation site for the α-phase formation in Zr-Nb (Ref 12, 46) and Ti-based alloys (Ref 18-21, 23, 42, 47). In this work, we observe the nanoscale ω or α-precipitates formed at the deformation process (see the SAED patterns presented in Fig. 4).

Starting from ~ 500 °C ($T\alpha_{EQ}$ in Fig. 5), a conventional α phase seems to precipitate, and a slight decrease in the dilatometry curve is observed. Another heat effect observed at 620 °C can be explained by eutectoid transformation of α-Zr to β-Zr according to binary phase diagram. During cooling the transformation of β-Zr into β-Zr + α-Zr mixture appears to start at temperature ~ 780 °C, but some fluctuations are also observed around the eutectoid temperature (610-650 °C).

3.2 Microhardness Behavior

Figure 6 compares dependencies of microhardness HV, diffraction peaks broadening β and residual macrostress σ_R on the UIT process time. It is seen that the main increment in hardness occurs on the first stage of the UIT processing (the treatment time for 60 s—till the extent of the effective stain becomes $\bar{e} \approx 0.2$). Further, the hardening rate decelerates, and then (after the UIT-2 process) it saturates with ongoing treatment. Compressive macrostresses σ_R increase with the UIT process time. The trend of the β dependence is almost identical to the HV curve indicating that β is sensitive to strain-induced changes of the microstructure (Fig. 4) and phase transformations (Fig. 5) in the UIT-modified surface layer. Moreover, the Williamson-Hall analysis confirms the prevailing role of the lattice microstrains $\langle \varepsilon^2 \rangle^{1/2}$ and negligible contribution of the size D of coherent scattering areas in the overall broadening of the diffraction profiles. These data correlate well to the TEM observations (Fig. 4).
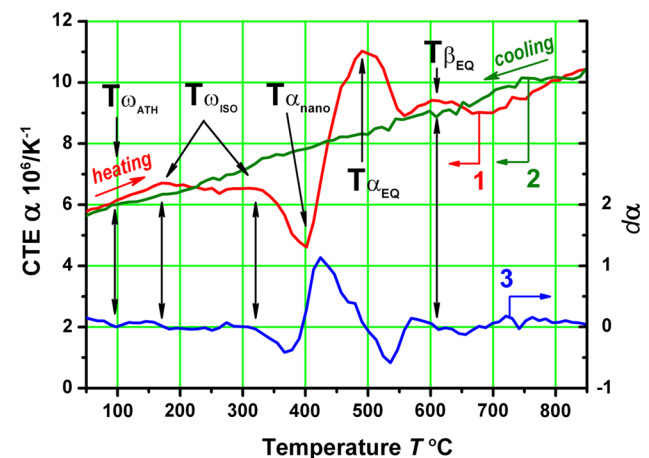

Fig. 5 Variations of the coefficient of thermal expansion α of the UIT-processed Zr-18%Nb alloy on heating (1) and cooling (2) and derivative Δα (3) on heating (heating rate 5 °C min^{-1})
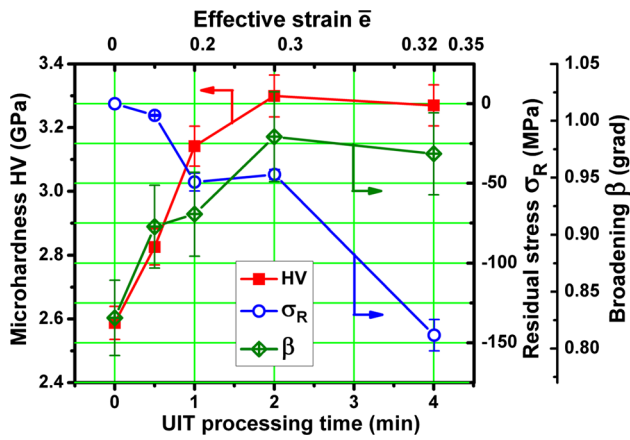
Fig. 6 Dependencies of measured microhardness HV and XRD estimated peak broadening β and residual stresses σ_R of the Zr-18%Nb alloy on the UIT process time

Fig. 7 Corrosion curves of the Zr-18%Nb alloy after different UIT regimes: 120 s (1), 240 s (2) as compared to the initial WQ state (0) and the UIT-modified Zr-1%Nb alloy (3) (Ref 27). The inset shows the dependences of the corrosion potential and passivation region on the UIP regime

Considering the well-known hardening mechanisms and the XRD (Fig. 2) and TEM (Fig. 4) data obtained in this study we can admit that mainly dislocation strengthening $(\Delta\sigma_1 = \alpha_1 G\rho^{1/2})$ and Orowan's strengthening $(\Delta\sigma_2 = \alpha_2 Gbd^{-1})$ support the registered hardening of the studied alloy during the UIT process. These hardening mechanisms are associated with an intensive multiplication of dislocations, which movements are complicated owing to nanoscale ω-precipitates (both the athermal and strain-induced ones). Experimentally, the operation of these dislocation-related mechanisms is confirmed by the aforementioned lattice microstrains $\langle\varepsilon^2\rangle^{1/2}$, which mainly caused the broadening of the XRD profiles. The nanograins, microbands, high-density dislocation and twining structure were observed even on the near surface of the UIT-processed 2024 alloy (Ref 48), which were shown to improve its fatigue resistance (Ref 49). Conversely, the solid solution hardening $(\Delta\sigma_3 = \alpha_3 Gc^{1/2})$ and grain boundary hardening $(\Delta\sigma_4 = kd^{-1/2})$ are negligible owing to the close similarity of the atomic size of Zr and Nb and due to insignificant grain refinement because of low extent of plastic deformation applied. The above-listed expressions contain the dimensionless constants α_1, α_2 and α_3, which are close to unity; a constant k (N mm$^{-3/2}$), which characterizes the specific strength of the grain boundaries; a shear modulus G, a Burgers vector b, a dislocation density ρ, a grain size d and a concentration c of the dissolved Nb atoms. Additionally, the oxygen atoms and their complexes penetrated into the surface layer owing to the mechanically induced transport can also be considered as effective obstacles for dislocation movements, and they thus may lead to additional hardening (Ref 50, 51). Moreover, the oxide formation may also increase HV essentially (Ref 51). It is worth to emphasize that the HV values (~ 3.3 GPa) obtained are higher than that of the Zr-1%Nb alloy (~ 2 GPa) processed with UIT for the same time (and strain extent) (Ref 27). Additionally, the Zr-18%Nb alloy has lower Young modulus (~ 70 GPa) in comparison with that of the Zr-1%Nb alloy (~ 97.5 GPa).

The HV saturation observed for the Zr-18%Nb alloy seems to occur due to moderate intensity of the used UIT process. If the impact energy and total mechanical energy applied would be increased, a higher strain extent would then be accumulated and additional strengthening mechanisms like grain boundary
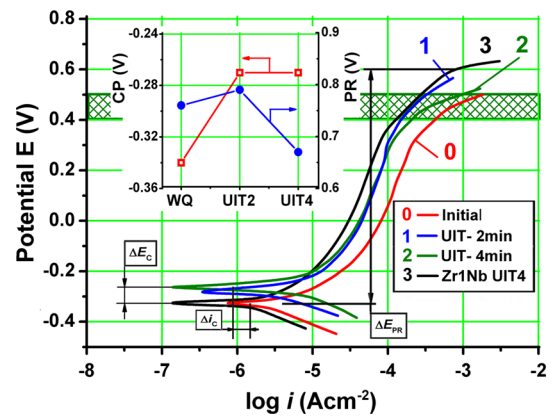
hardening would be involved. However, in this work, the applied mechanical energy was purposely chosen to have moderate value to prevent possible destruction of the oxide layer formed on the surface. Alternatively, such destruction would result in the formation of the composite layer with the broken oxide particles dispersed in the matrix alloy. The composite layer may still have enhanced hardness, but it also would be prone to corrosion attack. The corrosion behaviors of the UIT-modified specimens are discussed in the next subsection.

3.3 Corrosion Behavior

3.3.1 Polarization Characteristics. Potentiodynamic curves for anodic and cathodic polarizations of the WQ (curve 0) and UIT-modified (1.2) specimens are presented in Fig. 7. The obtained data are compared to the curve registered in the same electrochemical conditions for the Zr-1%Nb alloy modified with UIT4 (Ref 27). Polarization curves show that the UIT process improves the electrochemical performance of Zr-18%Nb alloy. After UIT the corrosion potential E_C increases becoming less negative. It is known that materials with more negative E_C generally experience more significant corrosion damage, whereas materials with a positive E_C (or less negative, as in our case) show higher corrosion resistance (Ref 52, 53). Corrosion current density i_C characterizing the degree of the material degradation at corrosion attack is lower for more corrosion resistant state (Ref 52). In our case, the latter state of Zr-18%Nb alloy is achieved after the UIT process, although the i_C decreased by more than a half of an order of magnitude.

Inset in Fig. 7 shows the decreased passivity region for the UIT4 specimen, which occurs owing to the increase in the corrosion potential E_C. The magnitudes of the breakdown potential E_{bd} related to the destruction of the passive film at the end of the passivity region (the beginning of the transpassive region) are also higher for the UIT-modified specimens. Considering the E_{bd} magnitudes registered for the Zr-18%Nb alloy after the UIT-1 and UIT-2 processes and their comparison with that of the UIT-modified Zr-1%Nb alloy (Ref 27) one can observe their close similarity. However, the E_{bd} is slightly higher for the latter alloy, i.e., the passive (oxide) film on the surface of the hcp Zr alloy has a slightly higher strength and

density than those formed on the bcc Zr-18%Nb alloy studied in this paper. It can be explained by the predominance of the (0001) hcp grains in the case of Zr1Nb alloy, which has close-packed lattice conversely to the bcc lattice of the Zr-18%Nb alloy. Nevertheless, the transpassive current increase on the curves registered for Zr-18%Nb alloy occurs within or higher the shaded area framed the interval of potentials between 0.4 and 0.5 V, which characterize the potentials appeared owing to the interaction of biological tissues and metallic biomaterials under physiological conditions (Ref 10). It confirms a possibility to use the modified alloy Zr-18%Nb in biomedical applications.

The compressive residual stresses observed in the UIT-treated specimens (open-circle curve in Fig. 6) can also play a beneficial role in the improvement of the corrosion behavior reducing pit formation on surface inclusions. A similar result was reported to 6082 aluminum alloy after laser peening in (Ref 52), where the modified aluminum oxide with more stable anodic behavior and higher pitting potential was revealed to be formed in the laser-treated area where the large compressive residual stresses were also observed. The UIT-processed specimens are believed to possess sufficiently stable surface integrity due to the large compressive stresses within the surface layer, and the oxide films formed onto the specimens during corrosion tests are more stable (demonstrating a higher E_{bd} potential for the start of transpassive region in the inset in Fig. 7) as compared to the initial specimen.

Generally, the passivity intervals are relatively clear for the studied samples, and a quite significant increase in the potentials associated with the formation of relatively large areas of the solid passive (oxide) film was observed for all the studied specimens at the current densities $i \approx -5$. During the passivity stage, the specimens also show higher ability to form passivation films and dense oxide layers that are noble with respect to the solution containing chlorine anions Cl^-. However, the depassivation processes occur simultaneously, which can be caused by the destruction of the oxide film and/or by the presence of iron atoms. Chlorine anions Cl^- can destroy passivation film or prevent its formation, and they also can facilitate the ionization of metallic ions connecting them in complexes. The iron cations with variable valence (Fe^{2+} and Fe^{3+}), which accumulated in the specimen surface after UIT (Fig. 8d), also activate the corrosion attack of the alloy. The Fe^{3+} ions having a higher degree of oxidation can participate in cathodic reactions accepting electrons ($Fe^{3+}+e \rightarrow Fe^{2+}$), or conversely, the Fe^{2+} ions having lower oxidation may interact with depolarizer (oxygen) accelerating the polarization (corrosion) again: $4Fe^{2+}+O_2+4H^+ \rightarrow 4Fe^{3+}+2H_2O$.

3.3.2 Surface Morphology. Figure 8 demonstrates the surface morphology of the Zr-18%Nb alloy in the original WQ state and after the UIT process carried out both on the air and argon environments. The morphologies of the WQ and argon-UIT-processed surfaces are almost similar with slightly higher gray areas in the latter specimen. Conversely, the air-UIT process mainly used in this study results in the formation of the oxide layers (Fig. 8c) and iron-containing islands (Fig. 8d) on the treated surfaces.

According to the EDX data (Fig. 9) the concentration of different admixtures, such as oxygen and iron, increases substantially in a surface layer. These changes seem to occur owing to the mechanically induced transfer of the oxygen and iron atoms during the UIT process similarly to those described for tantalum (Ref 32), titanium alloy Ti6Al4V (Ref 33),

Co28Cr6Mo alloy (Ref 34, 54), aluminum alloy (Ref 55) and hcp zirconium alloys (Ref 27, 28). The oxygen concentration increased substantially in the UIT-modified surface regardless the processing environment. However, it is naturally lower after the argon-UIT process (the specimen was blown by the argon stream). Conversely, the air-UIT process facilitates more intensive transport of the oxygen atoms into the surface layer forming the Zr-O solid solution (the oxygen concentration can be as high as 30%) (Ref 50, 51). Further, the ZrO_2 oxide islands can be formed and connected to the continuous oxide layer, which would be beneficial with regard to the enhancement of the anticorrosion properties of the modified surface. XRD analysis showed the formation of (ZrNbO)O oxide (Fig. 2). It was also reported that even at 300 °C the metastable β-Zr contained in Zr-2.5%Nb alloy oxidized to form a $Nb_2Zr_{x-2}O_{2x+1}$ oxide, which is structurally distinct from the monoclinic, tetragonal or cubic polymorphs of ZrO_2 (Ref 56). The enhanced corrosion resistance of the ZrO_2 oxide is well known (Ref 2, 57). However, heterogeneous phase state would deteriorate the strength and continuity of the oxide film (Ref 2). The cladding of iron can also occur at the UIT process (Ref 58) or SMAT (Ref 26). Additionally, the formation of the iron-containing islands can conversely facilitate suffering the alloy surface in corrosive media.

Thus, after analysis of the surface morphology and microstructural formations of the UIT-modified specimens the main origins intensifying the corrosion attack can be summarized. A number of factors should be accounted for. First of all, it is the presence of different chemical elements on the modified surface. The Fe atoms segregated on the alloy surface additionally to zirconium and niobium may form galvanic microcells. Thus, namely zirconium atoms having lower electrode potential ($E_{Zr^{4+}/Zr} = -1.53$ V versus $E_{Fe^{2+}/Fe} = -0.44$ V) would play a role of anodes in these electrolytic cells and will suffer the corrosion attack first.

The next factor is the formation of pores and damages in the oxide film that covers the metallic surface. When the oxide film loses its continuity, then the galvanic cells of another kind are formed. The parts of the oxide film will be cathodes in these galvanic cells, and the uncovered metallic surface playing a role of an anode will be corroded primarily.

Heterogeneous deformation accumulated during the UIT process also significantly affects the corrosive properties of the metallic material. Two metallic regions deformed to different strain extents will form another corrosive cell, which anode will be the more strained region of the metallic surface.

Finally, the precipitates and matrix material usually have different electrochemical properties, and thus can form the galvanic microcells of another kind. In the case of the Zr-18%Nb alloy, the β-phase matrix contains some volume fraction of ω- and α-precipitates after the UIT process. Therefore, more active dissolution of these precipitates or the β-phase matrix will depend on their electrochemical properties and on the cathodes/anodes formed in the appropriate galvanic microcells.

The texture, which is formed due to rolling followed by UIT, also affects the corrosion resistance of the surface layers, but in a positive manner. It is due to the fact that more close-packed lattice planes would have higher corrosion immunity (Ref 27, 28, 39). Another positive factor is the formation of continuous t-ZrO_2 oxide film providing high protection of the alloy from the corrosion attack in the saline solution.
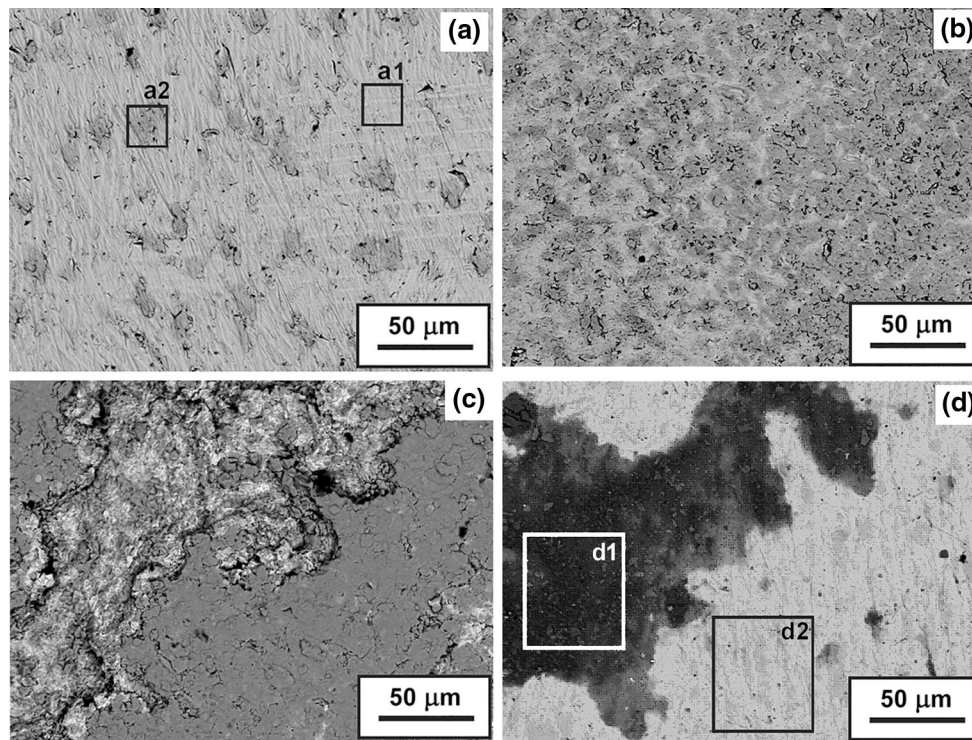
Fig. 8 SEM image of surface morphologies of Zr-18%Nb alloy in the initial WQ state (a) and after the argon-UIT (b) and air-UIT (c, d) processes
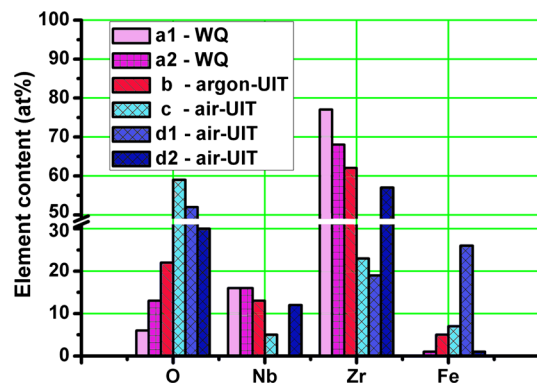
Fig. 9 Chemical compositions in the surface areas of Zr-18%Nb alloy indicated in Fig. 6 in the initial WQ state and after the argon-UIT and air-UIT processes

4. Summary

Near-surface layers in Zr-18%Nb alloy were modified using ultrasonic impact treatments (UIT) in this study. The effect of the UIT processing time on the microstructural formation, omega/alpha precipitations, microhardness and corrosion was analyzed. XRD analysis, TEM and SEM observations and EDX characterization allowed establishing the correlation between microstructure in the surface layers and their microhardness and corrosion resistance. The Zr-18%Nb alloy studied in this work demonstrates ∼ 1.5 times higher hardness, lower elastic modulus and better anticorrosion characteristics (less negative corrosion potential and lower corrosion current) in comparison with those of the UIT-processed Zr-1%Nb alloy, and thus it may have more potential in biomedical application. The following conclusions can be made:

1. Considering TEM observations, the microstructure in the near-surface layer at the strain extent up to $\bar{e} = 0.3$ mainly consists of tangled dislocations and their nets/bundles fixed with nanoscale ω- or α-precipitates seemingly promoted by multiple dynamic loads and the strain-induced temperature rise.
2. These data correlate well to the XRD observations indicating that the lattice microstrains play the prevailing role in the overall broadening of the diffraction profiles. Additionally, the XRD analysis reveals the intensive formation of zirconium (tetragonal-ZrO_2) and zirconium-niobium ((ZrNbO)O) oxides, moderate values of compressive residual stresses and {110} texture after the UIT process.
3. The main increment in hardness (to 3.3 GPa) occurs on the first stage of the UIT process (at the stain extent of $\bar{e}$ 0.2), and further, the hardness values saturate with ongoing treatment.
4. The enhancement of anticorrosion properties of the UIT-modified surface of Zr-18%Nb alloy in saline solution is facilitated by compressive residual stresses, {110} texture and oxidized surface containing both zirconium and zirconium-niobium oxides.

References

1. G.K. Dey and S. Banerjee, Decomposition of the β Phase in Zr-20%Nb, *J. Nucl. Mater.*, 1984, **125**(2), p 219–227

2. Y.H. Jeong, H.G. Kim, D.J. Kim, B.K. Choi, and J.H. Kim, Influence of Nb Concentration in the α-Matrix on the Corrosion Behavior of Zr-xNb Binary Alloys, *J. Nucl. Mater.*, 2003, **323**(1), p 72–80

3. R. Tewari, D. Srivastava, G.K. Dey, J.K. Chakravarty, and S. Banerjee, Microstructural Evolution in Zirconium Based Alloys, *J. Nucl. Mater.*, 2008, **383**(1–2), p 153–171

4. S. Cai, M.R. Daymond, A.K. Khan, R.A. Holt, and E.C. Oliver, Elastic and Plastic Properties of β_Zr at Room Temperature, *J. Nucl. Mater.*, 2009, **393**(1), p 67–76

5. S.K. Sahoo, V.D. Hiwarkar, L. Jain, I. Samajdar, P. Pant, G.K. Dey, D. Srivastava, R. Tewari, and S. Banerjee, Deformed Microstructures of Two-Phase Zr-2.5Nb Alloy: Effects of the Second Phase Hardness, *J. Nucl. Mater.*, 2010, **404**(3), p 222–230

6. T.P. Chernyaeva, V.M. Grytsyna, E.A. Mykhaylov, R.L. Vasilenko, and E.A.Slabospitskaya, Problems of Atomic Science and Technol., 2011, **2**(97), p 95–107, (in Russian)

7. N. Stojilovic, E.T. Bender, and R.D. Ramsier, Surface Chemistry of Zirconium, *Progr. Surf. Sci.*, 2005, **78**(3–4), p 101–184

8. L. Saldaña, A. Méndez-Vilas, L. Jiang, M. Multigner, J.L. González-Carrasco, M.T. Pérrez-Prado, M.L. González-Martín, L. Munuera, and N. Vilaboa, In Vitro Biocompatibility of an Ultrafine Grained Zirconium, *Biomaterials*, 2007, **28**(30), p 4343–4354

9. V. Braic, M. Balaceanu, M. Braic, C. Vitelaru, I. Titorencu, V. Pruna, A.C. Parau, and C. Fanara, Characterization of the Ti-10Nb-10Zr-5Ta Alloy for Biomedical Applications. Part 2: Wettability, Tribological Performance and Biocompatibility, *J. Mater. Eng. Perform.*, 2014, **23**(1), p 326–332

10. E. Eisenbarth, D. Velten, M. Müller, R. Thull, and J. Breme, Biocompatibility of β-Stabilizing Elements of Titanium Alloys, *Biomaterials*, 2004, **25**(26), p 5705–5713

11. B.A. Cheadle and S.A. Aldridge, The Transformation and Age Hardening Behaviour of Zr-19 wt%Nb, *J. Nucl. Mater.*, 1973, **47**(2), p 255–258

12. B.B. Straumal, A.S. Gornakova, A.A. Mazilkin, O.B. Fabrichnaya, M.J. Kriegel, B. Baretzky, J.-Z. Jiang, and S.V. Dobatkin, Phase Transformations in the Severely Plastically Deformed Zr-Nb Alloys, *Mater. Lett.*, 2012, **81**, p 225–228

13. YuF Bychkov, V.A. Ivanov, and A.N. Rozanov, Reversibility of β-ω Transformation in Zr-16%Nb Alloy, *Phys. Metals Metalloved.*, 1964, **17**(4), p 547–553 (in Russian)

14. S.L. Sass, The Structure and Decomposition of Zr and Ti b.c.c, *J. Less-Common Metals*, 1972, **28**(1), p 157–173 ((in Russian))

15. B.M. Mordyuk, O.P. Karasevska, P.E. Rudoi, I.O. Skyba, and H.H. Kamins'kyi, Influence of Ultrasonic Vibrations on the Phase Transformation and Strain Hardening of a Zr18Nb Alloy in Tension, *Mater. Sci.*, 2013, **48**(4), p 546–554

16. G.K. Dey, R. Tewari, S. Banerjee, G. Jyoti, S.C. Gupta, K.D. Joshi, and S.K. Sikka, Formation of a Shock Deformation Induced ω Phase in Zr20Nb Alloy, *Acta Mater.*, 2004, **52**(18), p 5243–5254

17. N.I. Khripta, B.N. Mordyuk, O.P. Karasevskaya, G.I. Prokopenko, and I.A. Skiba, Effect of Structural and Phase Transformations Induced by Ultrasonic Impact Peening on the Corrosion Resistance of Zr-based Alloys, *Metallofiz. Noveishie Tekhnol.*, 2008, **30**, p 369–382 (in Russian)

18. Y. Ohmori, T. Ogo, K. Nakai, and S. Kobayashi, Effects of ω-phase Precipitation on β → α, α″ Transformations in a Metastable β Titanium Alloy, Mater, *Mater. Sci. Eng., A*, 2001, **312**(1-2), p 182–188

19. E. Sukedai, D. Yoshimitsu, H. Matsumoto, H. Hashimoto, and M. Kiritani, β to ω Phase Transformation Due to Aging in a Ti-Mo Alloy Deformed in Impact Compression, *Mater. Sci. Eng., A*, 2003, **350**(1-2), p 133–138

20. M. Tane, T. Nakano, S. Kuramoto, M. Niinomi, N. Takesue, and H. Nakajima, ω Transformation in Cold-Worked Ti-Nb-Ta-Zr-O Alloys With Low Body-Centered Cubic Phase Stability and its Correlation With Their Elastic Properties, *Acta Mater.*, 2013, **61**(1), p 139–150

21. S. Nag, R. Banerjee, R. Srinivasan, J.Y. Hwang, M. Harper, and H.L. Fraser, ω-Assisted Nucleation and Growth of α Precipitates in the Ti-5Al-5Mo-5 V-3Cr-0.5Fe β Titanium Alloy, *Acta Mater.*, 2009, **57**(7), p 2136–2147

22. M. Ahmed, D. Wexler, G. Casillas, D.G. Savvakin, and E.V. Pereloma, Strain Rate Dependence of Deformation-Induced Transformation and Twinning in a Metastable Titanium Alloy, *Acta Mater.*, 2016, **104**, p 190–200

23. T. Gloriant, G. Texier, F. Sun, I. Thibon, F. Prima, and J.L. Soubeyroux, Characterization of Nanophase Precipitation in a Metastable β Titanium-Based Alloy by Electrical Resistivity, *Dilatometry Neutr. Diffr. Scrip. Mater.*, 2008, **58**(4), p 271–274

24. B.K. Kad, J.-M. Gebert, M.T. Perez-Prado, M.E. Kassner, and M.A. Meyers, Ultrafine-Grain-Sized Zirconium by Dynamic Deformation, *Acta Mater.*, 2006, **54**(16), p 4111–4127

25. T.A. Hayes, M.E. Kassner, D. Amick, and R.S. Rosen, The Thermal Stability of Surface Deformed Zirconium, *J. Nucl. Mater.*, 1997, **246**(1), p 60–69

26. P. Jiang, Q. Wei, Y.S. Hong, J. Lu, and X.L. Wu, In Situ Synthesis of Nanocrystalline Intermetallic Layer During Surface Plastic Deformation of Zirconium, *Surf. Coat. Technol.*, 2007, **202**(3), p 583–589

27. B.N. Mordyuk, O.P. Karasevskaya, G.I. Prokopenko, and N.I. Khripta, Ultrafine-Grained Textured Surface Layer on Zr-1% Nb Alloy Produced by Ultrasonic Impact Peening for Enhanced Corrosion Resistance, *Surf. Coat. Technol.*, 2012, **210**, p 54–61

28. B.N. Mordyuk, O.P. Karasevskaya, and G.I. Prokopenko, Structurally Induced Enhancement in Corrosion Resistance of Zr–2.5% Nb Alloy in Saline Solution by Applying Ultrasonic Impact Peening, *Mater. Sci. Eng., A*, 2013, **559**, p 453–461

29. S. Cai, M.R. Daymond, and R.A. Holt, Deformation of High β-Phase Fraction Zr-Nb Alloys at Room Temperature, *Acta Mater.*, 2012, **60**(8), p 3355–3369

30. L. Zhang and Y. Han, Twins Formation and Their Role in Nanostructuring of Zirconium, *Mater. Sci. Eng., A*, 2009, **523**(1-2), p 130–133

31. Y. Choi, E.J. Shin, and H. Inoue, Study on the Effect of Crystallographic Texture on the Corrosion Behaviour of Pilgered Zirconium by Neutron Diffraction, *Phys. B Condensed Matter.*, 2006, **385-386**(Part 1), p 529–531

32. P. Kar, K. Wang, and H. Liang, Force-Dominated Non-Equilibrium Oxidation Kinetics of Tantalum, *Electrochim. Acta*, 2008, **53**(16), p 5084–5091

33. M.A. Vasylyev, S.P. Chenakin, and L.F. Yatsenko, Ultrasonic Impact Treatment Induced Oxidation of Ti6Al4 V Alloy, *Acta Mater.*, 2016, **103**, p 761–774

34. Y.N. Petrov, G.I. Prokopenko, B.N. Mordyuk, M.A. Vasylyev, S.M. Voloshko, V.S. Skorodzievski, and V.S. Filatova, Influence of Microstructural Modifications Induced by Ultrasonic Impact Treatment on Hardening and Corrosion Behavior of Wrought Co-Cr-Mo Biomedical Alloy, *Mater. Sci. Eng., C*, 2016, **58**, p 1024–1035

35. B.N. Mordyuk, O.P. Karasevska, N.I. Khripta, G.I. Prokopenko, and M.A. Vasylyev, Structural Dependence of Corrosion Properties of Zr-1%Nb Alloy in Saline Solution, *Metallofiz. Noveishie Tekhnol.*, 2014, **36**(7), p 917–933. doi:10.15407/mfint.36.07.0917 ((in Russian))

36. B.N. Mordyuk, G.I. Prokopenko, M.A. Vasylyev, and M.O. Iefimov, Effect of Structure Evolution Induced by Ultrasonic Peening on the corrosion Behavior of AISI, 321 Stainless Steel, *Mater. Sci. Eng., A*, 2007, **458**(1–2), p 253–261

37. H. Hu, Texture of Metals, *Texture*, 1974, **1**(4), p 233–258

38. O.I. Zaporozhets, B.N. Mordyuk, N.A. Dordienko, V.A. Mykhailovsky, V.F. Mazanko, and O.P. Karasevska, Ultrasonic Studies of Texture in homogeneities in Pressure Vessel Steel Subjected to Ultrasonic Impact Treatment and Shock Compression, *Surf. Coat. Technol.*, 2016, **307**, p 693–701

39. Z. Pu, S. Yang, G.-L. Song, O.W. Dillon, Jr., D.A. Puleo, and I.S. Jawahir, Ultrafine-Grained Surface Layer on Mg–Al–Zn Alloy Produced by Cryogenic Burnishing for Enhanced Corrosion Resistance, *Scrip. Mater.*, 2011, **65**(6), p 520–523

40. M. Hoseini, A. Shahryari, S. Omanovic, and J.A. Szpunar, Comparative Effect of Grain Size and Texture on the Corrosion Behaviour of Commercially Pure Titanium Processed by Equal Channel Angular Pressing, *Corrosion Sci.*, 2009, **51**(12), p 3064–3067

41. S. Azimzadeh and H.J. Rack, Phase Transformations in Ti-6.8Mo-4.5Fe-1.5Al, *Metall. Mater. Trans. A*, 1998, **29**(10), p 2455–2467

42. F. Prima, P. Vermaut, G. Texier, D. Ansel, and T. Gloriant, Evidence of α-Nanophase Heterogeneous Nucleation from ω Particles in a β-metastable Ti-based Alloy by High-Resolution Electron, *Scrip. Mater.*, 2006, **54**(4), p 645–648

43. S. Nag, R. Banerjee, and H.L. Fraser, Microstructural Evolution and Strengthening Mechanisms in Ti-Nb-Zr-Ta, Ti-Mo-Zr-Fe and Ti-15Mo Biocompatible Alloys, *Mater. Sci. Eng., C*, 2005, **25**(3), p 357–362

44. P.Yu. Volosevich, G.I. Prokopenko, and B.N. Mordyuk, Evolution of Dislocation Structure at Impact Pulse Loads with Different Frequencies, *Metallofiz. Noveishie Tekhnol.*, 2000, **22**, p 61–71 ((in Russian))

45. A.V. Dobromyslov, N.I. Taluts, K.M. Demchuk, and A.N. Martemianov, Occurrence of β-ω Transformation in Zr-2.5%Nb Alloy at High Pressure, *Phys. Met. Metallogr.*, 1986, **62**, p 541–546 ((in Russian))

46. S. Neogy, K.V.M. Krishna, D. Srivastava, and G.K. Dey, A Study of Morphological and Compositional Evolution of Nanoprecipitates in the Zr-Nb System and Their Transformational Behavior, *Philos. Mag. A*, 2011, **91**(35), p 4447–4464

47. Z. Zhou, M. Lai, B. Tang, H. Kou, H. Chang, Z. Zhu, J. Li, and L. Zhou, Non-Isothermal Phase Transformation Kinetics of ω Phase in TB-13 Titanium Alloys, *Mater. Sci. Eng., A*, 2010, **527**(20), p 5100–5104

48. C.A. Rodopoulos, ATh Kermanidis, and ESh Statnikov, The Effect of Surface Engineering Treatments on the Fatigue Behavior of 2024-T351 Aluminum Alloy, *J. Mater. Eng. Perform.*, 2007, **16**, p 30

49. X. An, C.A. Rodopoulos, E.S. Statnikov, V.N. Vitazev, and O.V. Korolkov, Study of the Surface Nanocrystallization Induced by the Esonix Ultrasonic Impact Treatment on the Near-surface of 2024-T351 Aluminum Alloy, *J. Mater. Eng. Perform.*, 2006, **15**, p 355

50. A. Atrens, Dependence of the Pinning Point Dislocation Interaction Energy on the Dislocation Structure in Zirconium Oxygen Alloys, *Scrip. Mater.*, 1974, **8**(4), p 401–412

51. N.I. Khripta, Regularities of Formation of Structure-Phase States and Functional Properties of Zirconium Alloys in Conditions of Ultrasonic Impact Treatment, *Uspehi Fiziki Metallov*, 2016, **17**(2), p 119–152. doi: 10.15407/ufm.17.02.119

52. U. Trdan and J. Grum, Evaluation of Corrosion Resistance of AA6082-T651 Aluminium Alloy After Laser Shock Peening by Means of Cyclic Polarisation and EIS Methods, *Corrosion Sci.*, 2012, **59**, p 324–333

53. B.N. Mordyuk, G.I. Prokopenko, M.A. Vasylyev, and M.O. Iefimov, Effect of Structure Evolution Induced by Ultrasonic Peening on the Corrosion Behavior of AISI, 321 Stainless Steel, *Mater. Sci. Eng., A*, 2007, **458**(1–2), p 253–261

54. S.P. Chenakin, V.S. Filatova, I.N. Makeeva, and M.A. Vasylyev, Ultrasonic Impact Treatment of CoCrMo Alloy: Surface Composition and Properties, *Appl. Surf. Sci.*, 2017, **408**, p 11–20

55. M.A. Vasylyev, B.N. Mordyuk, S.I. Sidorenko, S.M. Voloshko, and A.P. Burmak, Corrosion of 2024 Alloy After Ultrasonic Impact Cladding with Iron, *Surf. Eng.*, 2017, doi:10.1080/02670844.2017.1334377

56. Y.P. Lin and O.T. Woo, Oxidation of β-Zr and Related Phases in Zr-Nb Alloys: an Electron Microscopy Investigation, *J. Nucl. Mater.*, 2000, **277**(1), p 11–27

57. G. Hunter, S.C. Jani, and V. Pawar, Method of Surface Oxidizing Zirconium and Zirconium Alloys and Resulting Product, US Patent, 2011, 7,896,926

58. M.A. Vasylyev, B.M. Mordyuk, S.I. Sidorenko, S.M. Voloshko, and A.P. Burmak, Mass Transfer During Ultrasonic Shock Treatment of Al-Fe, Metallofiz, *Metallofiz. Noveishie Tekhnol.*, 2015, **37**(12), p 1603–1618. doi:10.15407/mfint.37.12.1603 (in Ukrainian)